

Fatigue Behavior of Spot Welded High-Strength Sheet Steels

The spot weld fatigue properties of advanced automotive high-strength sheet steels were evaluated and compared to conventional sheet steels

BY R. W. RATHBUN, D. K. MATLOCK, AND J. G. SPEER

ABSTRACT. The fatigue behavior of spot welds was examined in three high-strength steels — HSLA 50, dual-phase 590, and TRIP 590 — and a lower-strength DQSK steel. Two sample geometries chosen to represent different loading conditions on the spot weld were evaluated. The specimen configurations included tensile-shear and cross tension. Spot welding was performed using standard industrial practices, although a two-step procedure was used for the higher-alloy TRIP grade. In both the tensile-shear and cross-tension tests, low- and intermediate-cycle fatigue lives increased with increased base material strength. Fatigue performance was found to be independent of strength and microstructure at high-cycle fatigue lives. In the cross-tension samples, which subjected the weld to crack opening (i.e., Mode I) loading, the TRIP material exhibited some interfacial fracture (brittle fracture along the weld centerline), and the presence of the interfacial fracture reduced the low-cycle (i.e., high-load) fatigue performance. At high cycles, the TRIP material performed equal to the other materials in both the cross-tension and tensile-shear samples. For all four materials, crack initiation occurred at a tongue structure at the sheet interface that results from molten material forced out from the weld nugget. The tongue structure was weakly bonded to the sheet surface, served as a precrack for fatigue, and nearly the entire fatigue life was spent in crack propagation. Crack propagation occurred through the heat-affected zone, with the crack path determined by stress distribution around the weld. No preferred microstructural path was evident. Fatigue data were analyzed using current fracture mechanics theories, and the results pro-

vided an accurate means of interpreting spot weld fatigue data between specimens of different geometries. Using stress intensity equations, spot weld fatigue data from other studies on steels with a wide range of strengths were also analyzed, and it was found that fatigue performance at high cycles was independent of base material strength and microstructure. It was confirmed that high-cycle fatigue performance is controlled by sample geometry alone, with no significant effect due to strength or microstructure.

Introduction

In the automotive industry, demand for greater fuel economy has created a continuing need for lighter-weight vehicles. One of the primary approaches to vehicle weight reduction is through downgauging of the sheet steels used in body structures where thinner gauges can be realized through the application of high-strength steels. In the recent Ultra Light Steel Auto Body Advanced Vehicle Concepts Project (Ref. 1), 100% of the body structure was designed from high-strength steels, resulting in a mass reduction of 20% compared to traditional designs.

Despite the trend toward other joining methods such as laser beam welding and adhesive bonding, spot welding remains the primary joining method for automotive structures, and the typical vehicle contains more than 3000 spot welds (Ref. 2). The fatigue behavior of spot welds continues to be an important factor in vehicle design.

Available fatigue data for spot welds were developed using previous genera-

tions of steels, i.e., low-carbon and HSLA sheet steels, typically with tensile strengths in the range of 200 to 600 MPa (29 to 90 ksi), and microstructures consisting primarily of ferrite and iron-carbide (typically in pearlite or as a dispersed second phase) (Ref. 3). In these investigations it was shown that spot weld fatigue performance is independent of base material strengths, and the primary variables that control fatigue performance are weld nugget size, sheet thickness, and the corresponding joint stiffness (Refs. 4, 5). However, low-carbon and HSLA steels are being replaced increasingly with newly developed multiphase or complex-phase sheet steels, such as dual-phase and TRIP steels, having tensile strengths of about 600 MPa (90 ksi) or greater. These steels have microstructures consisting of a combination of ferrite, martensite, retained austenite, and bainite, and have been the subject of numerous recent publications (e.g., Ref. 6). Given that the majority of the fatigue life is spent propagating the crack through the microstructure (Ref. 7), changes in microstructural strengthening mechanisms could result in significant changes in fatigue life. Thus, there is a need to examine the fatigue performance of spot welds made in newly developed high-strength products.

As summarized in a recent overview of new automotive sheet steels (Ref. 8), conventional low-carbon automotive sheet steels are typically processed by hot- and cold-rolling, followed by recrystallization annealing at temperatures where austenite formation is avoided or cooling is controlled to retransform any austenite at high temperature to a predominantly ferritic microstructure. In contrast, after cold-rolling, dual-phase (DP) and TRIP steels are processed by intercritical annealing followed by lower-temperature transformation of the austenite. The choice of intercritical annealing temperature determines the relative volume-fractions of ferrite and austenite at temperature, and the time-temperature history during cooling controls the final microstructure. If the steel is rapidly cooled

KEY WORDS

Automotive Industry
Fatigue Resistance
Sheet Steel
Spot Welding
Tensile-Shear Strength

R. W. RATHBUN, was with the Advanced Steel Processing and Products Research Center, Colorado School of Mines, Golden, Colo., at the time this work was done. He is currently with QuesTek Innovations, Evanston, Ill. D. K. MATLOCK (303-273-3016), and J. G. SPEER are with the Advanced Steel Processing and Products Research Center, Colorado School of Mines, Golden, Colo.

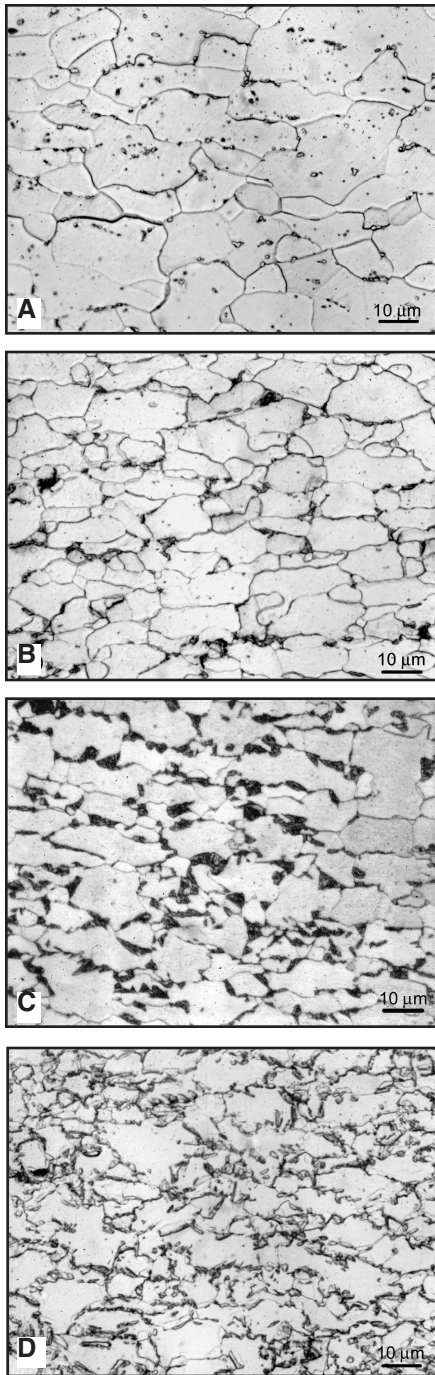


Fig. 1 — Light optical micrographs of base material microstructures. A — DQSK; B — HSLA; C — DP; D — TRIP. 2% nital etch.

to ambient temperature from the intercritical annealing temperature, then the austenite undergoes a martensitic transformation resulting in a DP steel, consisting primarily of ferrite and martensite with small amounts of retained austenite, and the mechanical properties are controlled by the martensite volume-fraction and ferrite grain size (Ref. 9). For appropriately designed steel compositions, if cooling after intercritical annealing is arrested and transformation is accom-

Table 1 — Compositions (wt-%) and Calculated Carbon Equivalent (CE) of Experimental Materials (Ref. 13)

Material	C	Mn	P	S	Si	Cr	Al	Cb/Nb	CE
DQSK	0.023	0.23	0.006	0.015	—	—	—	—	0.06
HSLA 50	0.05	0.39	0.011	0.008	0.02	0.03	0.039	0.029	0.12
DP 590	0.088	1.00	0.01	0.006	0.31	0.02	0.053	—	0.28
TRIP 590	0.083	1.52	0.078	0.007	1.08	0.03	0.039	0.001	0.42

plished at an intermediate temperature, then microstructures consisting of bainitic ferrite with larger quantities of austenite can also be obtained after final cooling to room temperature. These products are referred to as “TRIP” sheet steels because the austenite can transform to martensite during deformation encountered in manufacturing (e.g., forming) or in service, according to the well-known “TRansformation Induced Plasticity” phenomenon (Ref. 10). The mechanical properties of TRIP steels depend on the volume-fraction, morphology, and distribution of the retained austenite, along with the volume-fractions and properties of the bainitic ferrite and equiaxed ferrite constituents (Refs. 6, 11).

Dual-phase and TRIP steels are alloyed to control the amount and transformation of intercritically formed austenite. The carbon content in these steels is typically in the range of 0.05 to 0.2 wt-% C, and the manganese content may be up to approximately 1.5 wt-%. In TRIP steels, Si or Al additions are also made to limit cementite formation, thus enhancing the amount of retained austenite present after isothermal transformation, and P may be added as a ferrite solid-solution strengthener (Ref. 12). As a consequence of alloy additions, the carbon equivalents for DP or TRIP grades are typically higher than those for conventional low-carbon sheet steels. During spot welding it is anticipated that the weld thermal cycle will significantly modify the DP and TRIP steel microstructures in the heat-affected zone. Furthermore, the higher alloy contents in these steels will potentially lead to higher strengths in the spot weld nuggets, and welding procedures may need to be modified to account for the higher carbon equivalents (Ref. 13).

The purpose of this work is to evaluate the effects of spot welding on microstructures and fatigue behavior of DP and TRIP steels of current interest in automotive manufacture. Data are obtained on two different specimen geometries and are compared to data obtained on a ferrite-pearlite HSLA steel and a conventional low-carbon DQSK steel. A methodology is also developed to directly compare data obtained in this study with spot weld fatigue data obtained previously.

Experimental Procedure

Three high-strength steels, utilizing dual-phase, TRIP, and HSLA microstructures, were chosen for this study. To serve as a baseline for comparison, a low-strength Drawing Quality Special Killed (DQSK) material was also tested. To facilitate comparison between materials, steels of similar strengths and thicknesses were used. The specific steel grades chosen for this study are HSLA 50, dual-phase 590, and TRIP 590. Note that the “50” in HSLA 50 refers to the minimum yield strength in ksi and the “590” in DP 590 and TRIP 590 refers to the minimum ultimate tensile strength in MPa. The chemical compositions and carbon equivalents ($CE = \%C + \%Mn/6 + (\%Cr + \%V)/5 + \%Si/15$) (Ref. 14) are summarized in Table 1. The DQSK steel is a conventional low-carbon (0.023 wt-% C) steel; the HSLA 50 steel has a slightly higher carbon content and is microalloyed with Nb; and the DP and TRIP steels have higher C and Mn additions. Note that the TRIP steel is also alloyed with Si (1.08 wt-%) and P (0.008 wt-%). The DQSK and HSLA steels were obtained as 1.5-mm (0.060-in.)-thick sheets, and the dual-phase and TRIP steels were obtained as 1.4 mm (0.055-in.)-thick sheets.

Substrate, weld metal, and heat-affected zone microstructures were evaluated with standard metallographic techniques with samples etched in 2% nital. Figure 1 shows the as-received microstructures of the four experimental steels. The DQSK steel (Fig. 1A) consists of coarse ferrite grains with a uniform dispersion of fine carbides; the HSLA steel (Fig. 1B) consists of fine-grained ferrite along with dark-etching pearlite colonies. Consistent with the description of these materials in the introduction, the DP steel (Fig. 1C) consists of ferrite with dark-etching martensite, and the TRIP steel (Fig. 1D) consists of ferrite with finely dispersed austenite (approximately 6%) and transformed austenite (e.g., martensite and/or bainite).

Room-temperature longitudinal and transverse tensile properties of the materials were evaluated using standard ASTM E-8 specimens at a strain rate of 0.00167 s^{-1} , and the results are summarized

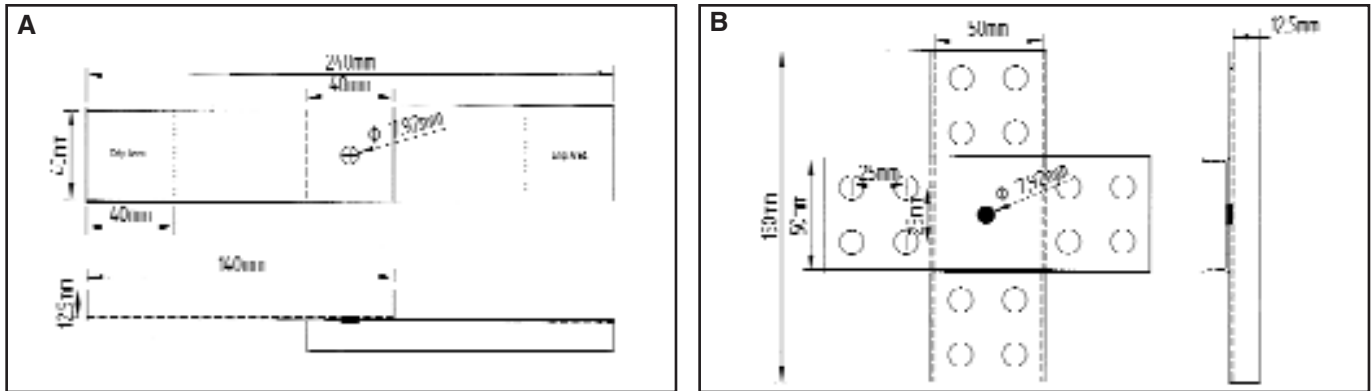


Fig. 2 — Dimensions of samples: A — tensile-shear; and B — cross tension.

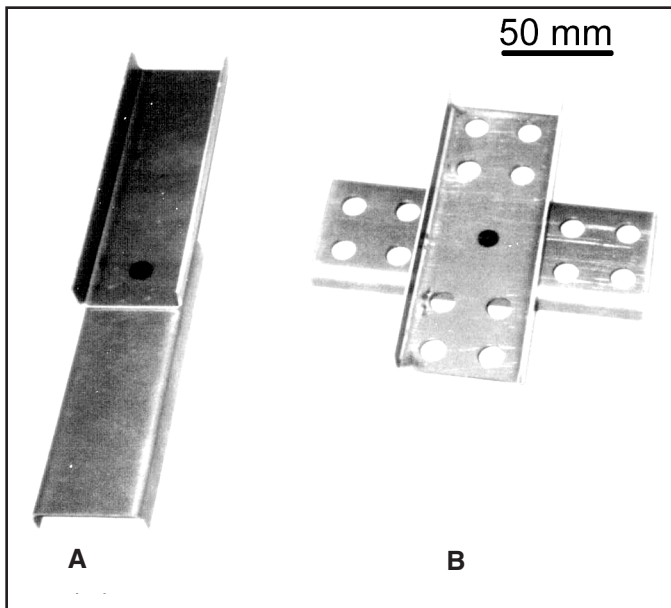


Fig. 3 — Photograph of experimental test samples: A — tensile-shear; and B — cross tension.

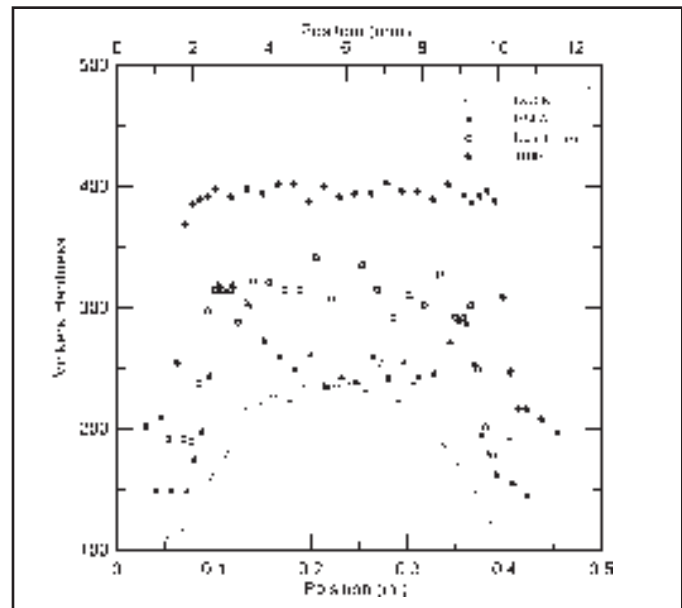


Fig. 4 — Microhardness profiles of representative welds from each of the four experimental materials.

in Table 2. All materials exhibit properties consistent with their representative material class. The properties of each material are nearly the same in each orientation, with the exception of HSLA 50, which has higher yield and tensile strengths in the transverse direction.

For this study, uncoated material was preferred in order to potentially prevent complications from zinc embrittlement effects during welding. The HSLA material was received with a galvanized coating, the TRIP material was received with an electrogalvanized coating, and the other two steels were obtained in the uncoated condition. Prior to welding, the zinc-based coatings were removed using a 5% HCl solution with 0.15% Thiourea inhibitor. Tension testing verified that the stripping process did not alter the mechanical properties of the material (Ref. 15).

Table 2 — Longitudinal (L) and Transverse (T) Tensile Properties of As-Received Materials

Specimen	Yield Strength MPa (ksi)	Tensile Strength MPa (ksi)	Total Elongation (%)
DQSK — L	200 (29)	340 (49)	44
DQSK — T	200 (29)	340 (49)	42
HSLA 50 — L	350 (50)	420 (62)	30
HSLA 50 — T	400 (58)	450 (66)	28
DP 590 — L	350 (51)	620 (90)	28
DP 590 — T	360 (52)	630 (92)	28
TRIP 590 — L	430 (63)	610 (88)	32
TRIP 590 — T	430 (63)	610 (88)	33

During service, spot welds in automotive structures are subjected to complicated loading histories. Spot welds can experience both shear loading due to relative displacement or rotation of adjacent sheets, and tensile loading due to separating forces applied between adjacent sheets in a direction normal to the sheets.

The test specimen configurations used in this study were chosen to evaluate the fatigue performance of spot welded material in two loading conditions: shear only and tensile only. The specimens used to test the spot welds in shear and in tension are based on the JIS Z 3138 tensile-shear and cross-tension specimens, respectively

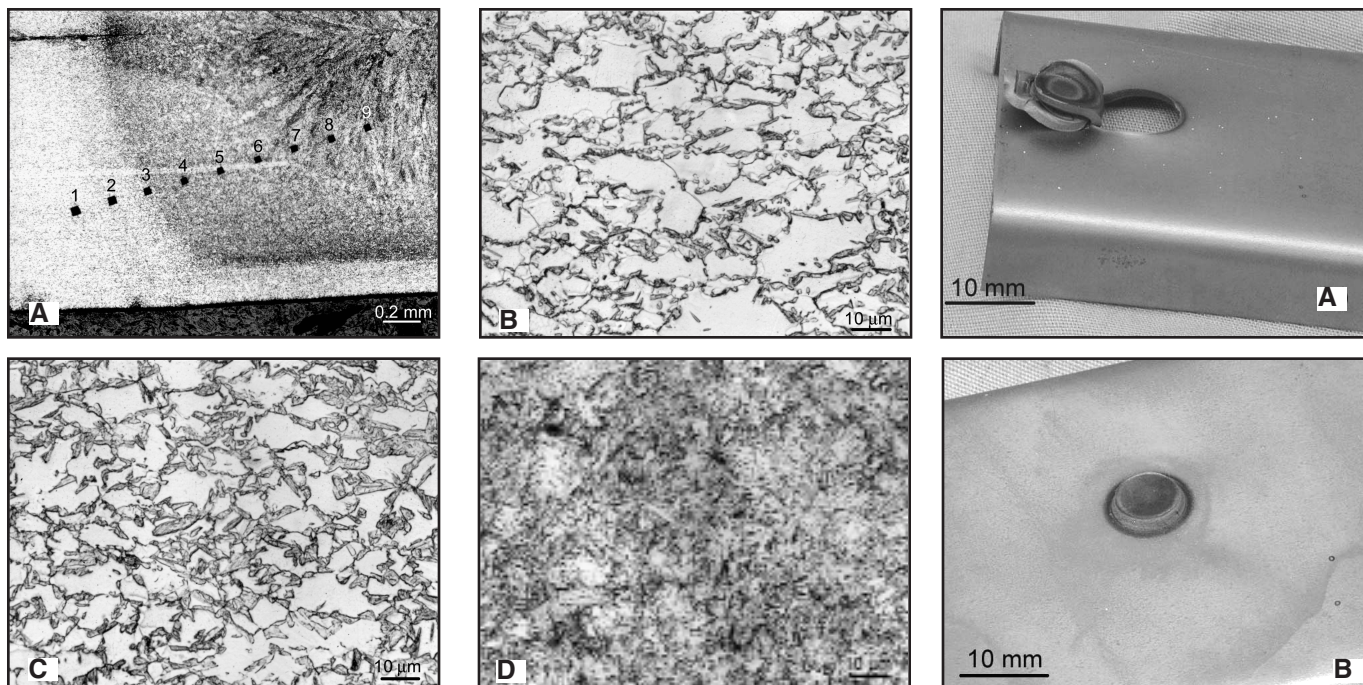


Fig. 5 — Photomicrographs of TRIP spot weld HAZ; A — with microhardness indentations; B — point #2, 238 HVN, 24% hard constituent; C — point #3, 302 HVN, 35% hard constituent; D — point #4, 396 HVN, 84% hard constituent. 2% nital etch.

(Ref. 16). To control loading in each of these configurations more precisely, flanges were added to the edges of the specimens to reduce sheet bending and nugget rotation. The sample dimensions are summarized in Fig. 2, and a photograph of the actual samples is in Fig. 3. Both sample geometries were gripped with fixtures that utilized a universal joint attached to the upper grip to facilitate alignment. The cross-tension samples were bolted to rigid assemblies designed to span the four-hole patterns on each beam (Ref. 15).

Spot welding was performed using a pedestal-type spot welding machine rated at 75 kVA at 440 V, controlled by a PLC. The electrodes used were a Cu-Cr Class 2 truncated cone, turned and faced on a lathe to the required diameter. Standard automotive production welding schedules were used (Ref. 17) and adjusted appropriately for each material. An electrode face diameter of 7.9 mm (0.31 in.) was used, and the current was adjusted to produce consistent full-face-diameter welds without expulsion. For the DQSK steel, the electrode force was 900 lb (4 kN). The force was increased by 10% to 990 lb (4.4 kN) for the high-strength materials. For the TRIP 590 material, it was found that full-face-diameter welds could not be produced without expulsion using a single-pulse weld schedule. Therefore, a dual-pulse method was used, with two weld pulses of 9 cycles separated by a hold time of 1 cycle. The electrode force was further

increased to 1100 lb (4.9 kN) for the TRIP 590 steel. The final weld schedules are summarized in Table 3.

Monotonic strength tests and fatigue testing of welded specimens were carried out on commercial servo-hydraulic axial test frames. Monotonic strength tests were executed in displacement control at a rate of 0.2 in./min (0.085 mm/s). Load and actuator displacement were continually measured throughout the tests. Fatigue testing was performed in force control using a sine wave at 10 Hz and a 0.1 load ratio. For the cross-tension specimen, actuator displacements at peak and minimum load were periodically recorded, allowing an effective compliance measurement. Compliance data on the tensile-shear specimens were measured using a 2-in. (50.8-mm) clip gauge.

Results and Discussion

Weld Characterization

Welds from each material were sectioned for hardness testing, and the resulting microhardness traverses are shown in Fig. 4. For each material, the microhardness at the left side of each plot is representative of the base metal hardness. All materials exhibited a significant hardness increase in the weld. The transition in hardness from the base material to the weld differed somewhat between materials. For the DQSK material, there was a gradual increase in hardness through the

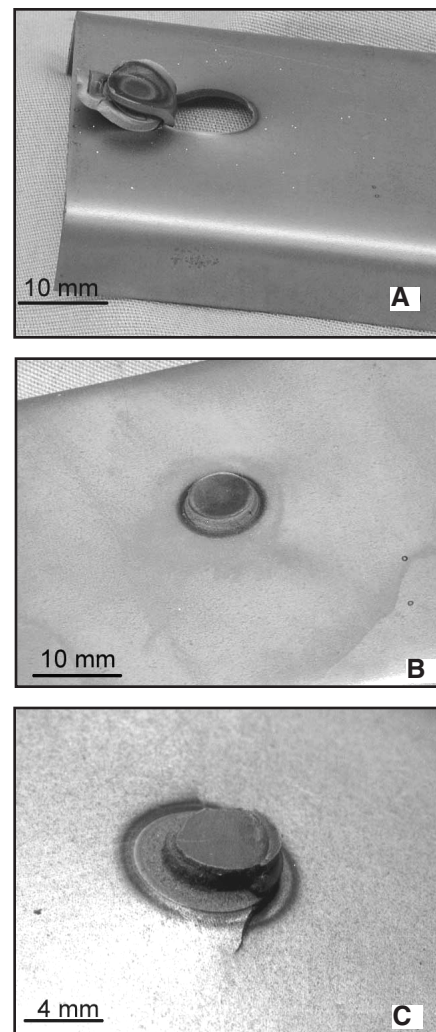


Fig. 6 — Weld failures in monotonic overload. A — DP 590 tensile-shear sample showing plug-type failure and resulting fold-over. B — Plug failure in a DP 590 cross-tension sample. C — Interfacial fracture of TRIP steel in cross-tension loading. For reference, weld is approximately 6 mm in diameter.

heat-affected zone (HAZ) into the weld metal, with a hardness increase from approximately 110 to 225 HVN. In contrast, the hardness change through the heat-affected zone was sharp for all three high-strength steels. The HSLA and DP steels have similar hardness profiles through the HAZ, with a peak in hardness of approximately 320 HVN. Owing to the higher alloy content, the weld metal hardness of the TRIP steel was the highest at approximately 400 HVN. No significant softening was observed in the HAZ of any of the materials.

The relative diameters of the welds in each material are also apparent in Fig. 4. Quantitative measurements of weld size were obtained from button diameter on peel coupons. The DQSK steel had the smallest weld button, with an average di-

iameter of 7.6 mm (0.30 in.). The weld diameters in the HSLA and DP steels were nearly identical, though slightly larger than those in the DQSK, with average diameters of 7.9 mm (0.31 in.) and 8.0 mm (0.31 in.) respectively. Due to the dual-pulse welding method employed, the TRIP steel has the largest average weld diameter at 8.4 mm (0.33 in.).

Figure 5 presents a series of light optical micrographs that illustrate the variation in microstructure across the HAZ of the TRIP steel and is presented here to illustrate the types of microstructural variations observed in all welds. A complete summary of micrographs from the other steels is presented elsewhere (Ref. 15). Figure 5A includes a low-magnification

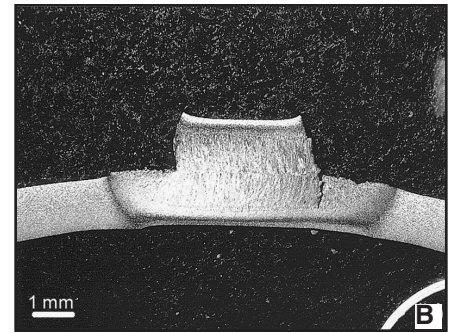
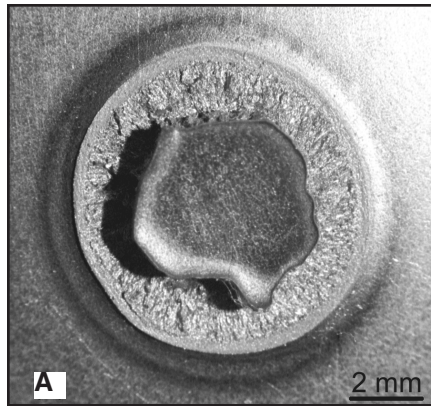


Fig. 7 — Photographs of TRIP spot weld failed in overload showing presence of interfacial fracture. A — Macro photograph of a normal view. B — Light optical micrograph of a transverse view. 2% nital etch.

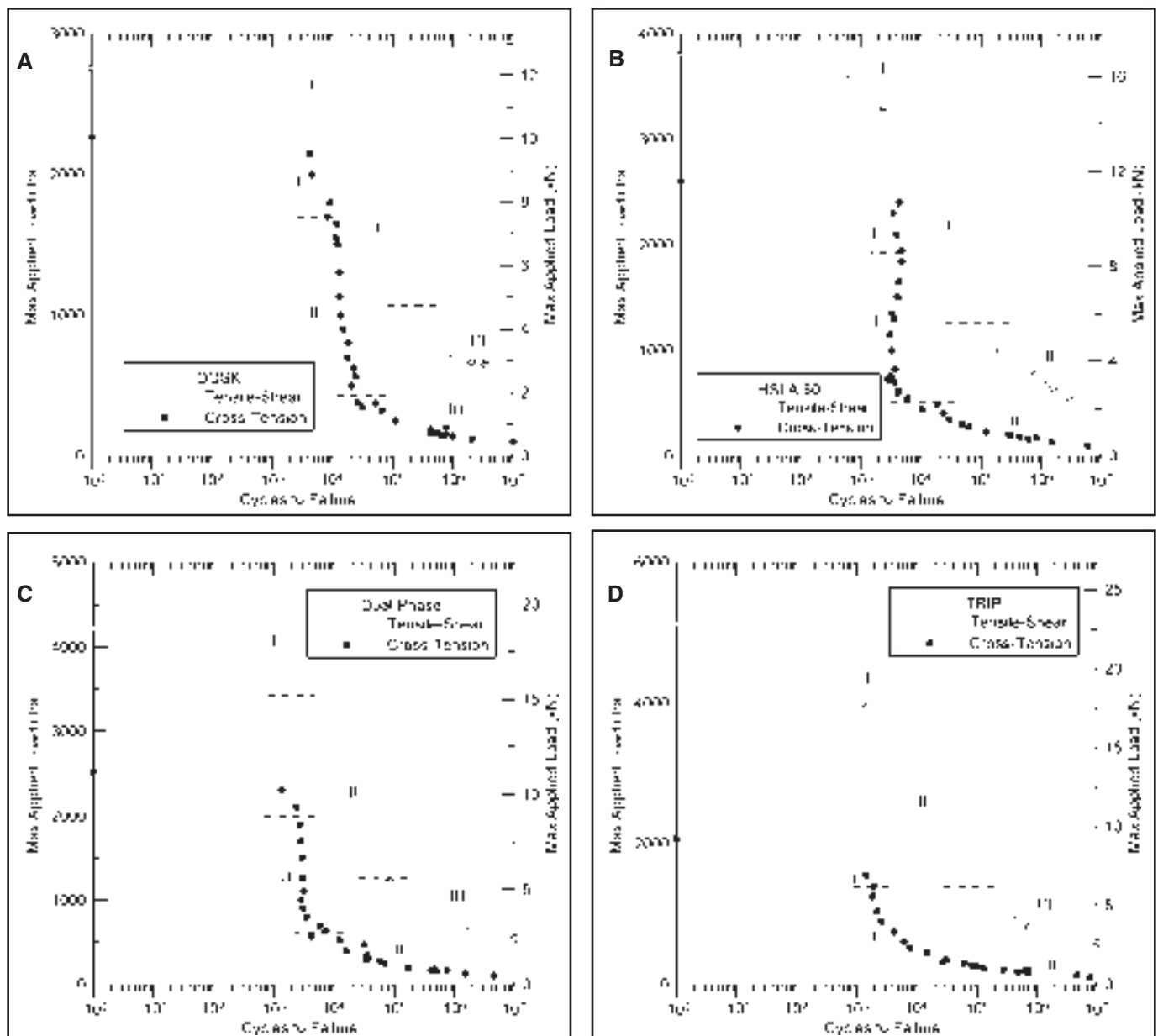


Fig. 8 — Load vs. cycles to failure for the four experimental materials in the cross-tension and tensile-shear configurations. A — DQSK; B — HSLA 50; C — DP; and D — TRIP steels.

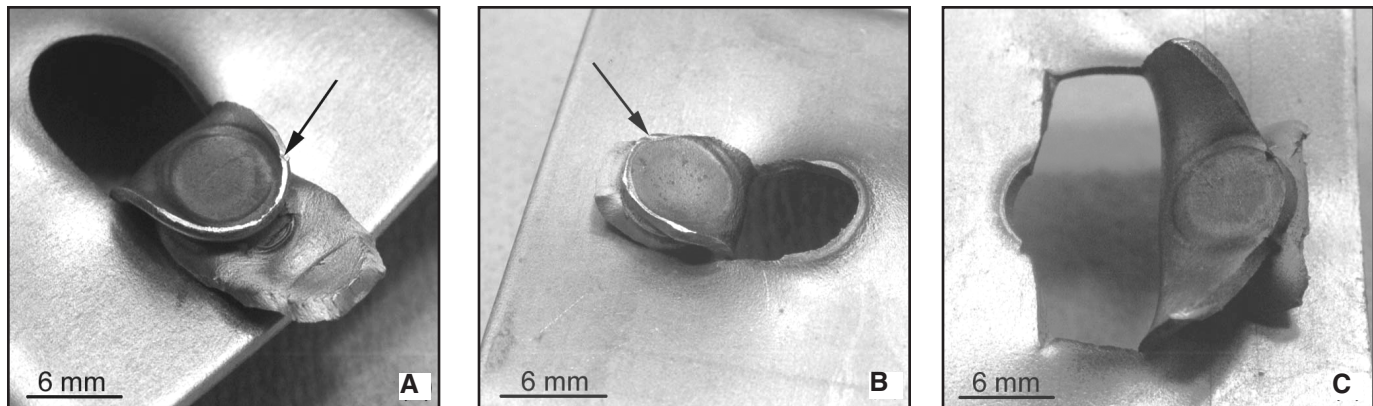


Fig. 9 — Tensile-shear fatigue failure modes: A — Type I failure, notice plastic deformation surrounding weld button, DQSK tested at 2600 lb, 1000 cycles; B — Type II failure, DQSK tested at 2400 lb, 4000 cycles; C — Type III failure, DQSK tested at 850 lb, 510,000 cycles.

Table 3 — Weld Schedules Used to Spot Weld the Materials in this Study

Material	Force (lb)	Squeeze (cycles)	Weld (cycles)	Hold (cycles)	Avg. Weld Current (kA)	Expulsion Current (kA)
DQSK	900	90	12	5	12.2	12.4
HSLA 50	990	90	12	5	12.3	12.4
DP 590	990	90	12	5	11.5	11.54
TRIP 590	1100	90	9/9	5	10.4/10.6	10.89

view of the base metal, HAZ, and weld metal. Also shown in Fig. 5A are numbered microhardness indentations that serve to reference the positions of the higher-magnification micrographs presented in Fig. 5B to 5D. The micrographs in Fig. 5B to 5D were chosen to illustrate the microstructural variations observed within the HAZ where the hardness gradient was a maximum. The microstructure in Fig. 5B is within the tempered region (see Fig. 5A) of the HAZ and is essentially equivalent to the as-received base metal. Figure 5C shows a region of increased hardness at the edge of the darker-etching portion of the HAZ where the volume-fraction of the martensite/austenite constituent (and corresponding hardness) are increased over the base metal, indicating that this region was intercritically heated (i.e., to a temperature above the A_1). At location #4 (see Fig. 5A), Fig. 5D indicates the material was heated above the A_3 as the microstructure is primarily martensite (approximately 84%) with a hardness equivalent to the weld nugget. Similar localized microstructural variations were observed in welds of the other three steels (Ref. 15).

Weld Strength

Static weld strength tests were performed on tensile-shear and cross-tension samples for each material and configura-

tion. The maximum weld loads are summarized in Table 4 and the ratios of the weld strengths as normalized by the bead areas to the base metal ultimate tensile strengths are summarized in Table 5. For the tensile-shear samples, the weld strength increases with base metal tensile strength, and, as summarized in Table 5, the ratios of weld strength to base metal tensile strength are approximately constant. In contrast, for the cross-tension samples, the ratios of weld to base metal tensile strength for the DP and TRIP steels are significantly lower, indicating the severity of the tensile loading condition associated with the cross-tension sample.

For both specimen geometries, all materials exhibited a fracture morphology that was essentially of the “plug type,” where the weld button remained intact and pulled out from one sheet. In the tensile-shear configuration, the weld nugget was torn from both sheets and folded over, as shown in the photograph of a representative failure in Fig. 6A. For the DQSK, HSLA, and dual-phase materials in the cross-tension configuration, the weld completely separated from one sheet, as shown by the DP steel specimen in Fig. 6B. However, due to its higher alloy content, the TRIP material failed interfacially, as discussed below. A view of the weld button in the TRIP steel after interfacial fracture is shown in Fig. 6C. The weld shown

Table 4 — Ultimate Strengths of Welds in Tensile-Shear and Cross-Tension Configuration

Material	Tensile-Shear kN (lbf)	Cross-Tension kN (lbf)
DQSK	12.3 (2760)	10.1 (2270)
HSLA 50	16.9 (3800)	11.6 (2600)
DP 590	18.7 (4220)	11.2 (2520)
TRIP 590	22.8 (5130)	9.2 (2070)

has approximately 30% interfacial fracture, which is typical for this steel in cross-tension loading, and leads to the low maximum load value shown in Table 4.

The hardenability associated with the high alloy content in the TRIP steel resulted in the formation of a notch-sensitive martensitic microstructure in the weld, and the triaxial stress state of the cross-tension test promoted interfacial fracture of the weld. As shown in Fig. 7, which includes normal (Fig. 7A) and transverse (Fig. 7B) views of a cross-tension weld failed in overload, the interfacial fracture surfaces of the TRIP steels used in this study consisted of an annular ring of microvoids around an area of brittle fracture that was primarily intergranular. It should be noted that the extent of brittle fracture observed for the TRIP steel here is similar to the behavior reported for spot welds in TRIP steel processed with welding histories designed to optimize spot weld properties (Ref. 13). While others (Ref. 18) have interpreted the microvoids as microporosity associated with phosphorus in the weld metal, the specific fracture mechanism associated with the annular ring was not clarified here.

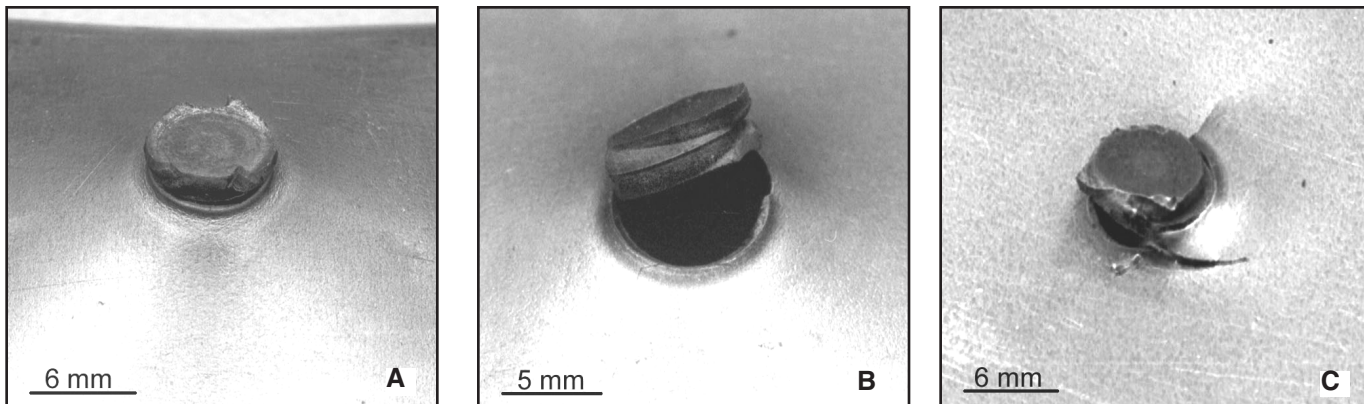


Fig. 10 — Cross-tension failure modes: A — Type I failure, DQSK tested at 2150 lb, 4200 cycles; B — Type II failure, weld has rotated up out of base sheet, DQSK tested at 900 lb, 15,000 cycles; C — Type III failure, notice cracks extending from weld into base material, DQSK tested at 190 lb, 420,000 cycles.

Table 5 — Ratio of Weld Tensile Strength, Estimated from Hardness, to Base Material Tensile Strength

Material	Weld Hardness (HVN)	Est. Weld Strength (ksi)	Base Material Strength (ksi)	Ratio Weld/Base
DQSK	225	103	49	2.1
HSLA	320	150	64	2.3
Dual Phase	320	150	91	1.6
TRIP	400	190	88	2.2

Fatigue Testing

Complete cross-tension and tensile-shear fatigue life curves are shown for all materials in Fig. 8. Each datum point represents the result from a single test, and the points plotted at 10^0 cycles correspond to the single-cycle overload strengths from Table 4. As evidenced by the limited scatter in cycles to failure, excellent reproducibility between samples was obtained, and each data set could be characterized by a smooth curve. For each material, data for the tensile-shear samples plotted above the corresponding data for the cross-tension samples. For each sample geometry, the general curve shape was similar for all four materials, and the fatigue resistance, as measured by the applied load, decreased markedly in the range of 10^3 to 10^4 cycles. In this range, the decrease in fatigue resistance for the cross-tension samples is more dramatic than for the tensile-shear samples, and the DP and TRIP sheet steels actually exhibit a decrease in life with a decrease in load. This apparently anomalous behavior is discussed further below.

Three distinctive failure modes were identified in both the tensile-shear and cross-tension configurations, and representative photographs of fractured welds are presented in Figs. 9 and 10 for the ten-

sile-shear and cross-tension configurations, respectively. These failure modes were correlated to distinct features of the fatigue curves, and dashed horizontal lines in Fig. 8 indicate the transition loads between regions as identified from visual analysis of failed fatigue samples. In each configuration, “Type I” corresponds to the relatively flat high-load portion, “Type II” corresponds to the steep transition region, and “Type III” corresponds to the flatter low-load, long-life portion of the curve. For the tensile-shear specimen, the Type I failure mode is a plug failure with a surrounding ring of plastically deformed material, as indicated by the arrow in Fig. 9A. For Type II, the fatigue crack propagated through the sheet thickness and along the circumference of the weld button, resulting in a plug failure without the ring of deformed material (see arrow in Fig. 9B). In Type III failure mode, the fatigue crack propagated around approximately 25% of the circumference and then propagated into the base sheet along a plane of maximum tension (Fig. 9C).

In the cross-tension configuration, the Type I failure was a complete plug failure as shown in Fig. 10A, with substantial deformation in the base sheet. For Type II, the fatigue crack penetrated the thickness in both sheets, resulting in weld separation and rotation of the button, as shown in

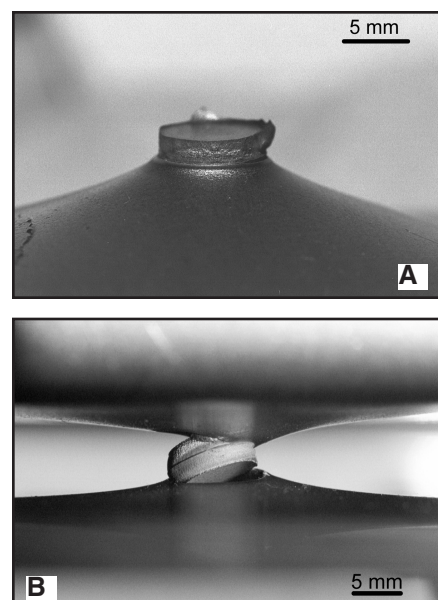


Fig. 11 — Macrophotographs of fatigue failure in DQSK steel cross-tension fatigue samples: A — Type I, tested at 2000 lb, 4450 cycles-to-failure; B — Type II, tested at 375 lb, 50,600 cycles-to-failure.

Fig. 10B. For Type III, the weld rotated out of plane similar to Type II, and the button rotation was followed by crack propagation into the base sheet — Fig. 10C. Further evidence for the difference in the failure geometry between Type I and Type II failure is presented in the macrophotographs of failed dual-phase steel welds in Fig. 11. Figure 11A, a transverse view of a Type I failure, shows the extensive base metal deformation associated with fatigue failure at high loads. Figure 11B shows the weld button rotation and through-thickness crack propagation around the circumference of the weld.

The fracture types shown in Figs. 9 to 11 were identified by direct visual evaluation of weld buttons after testing. The

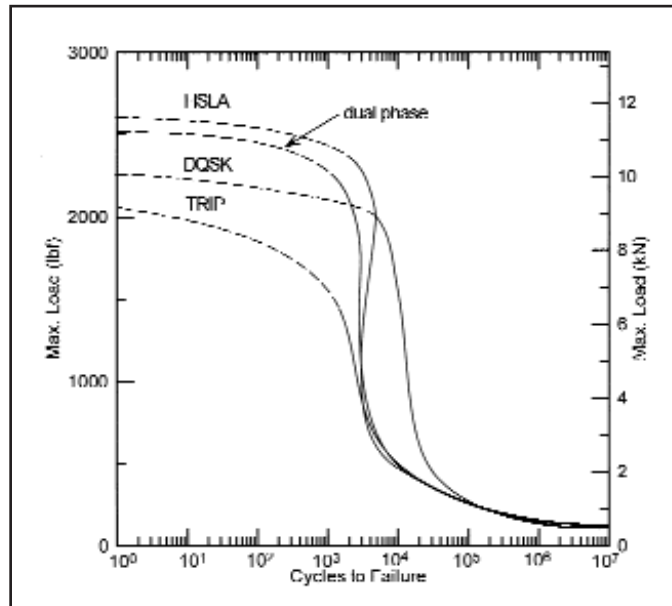
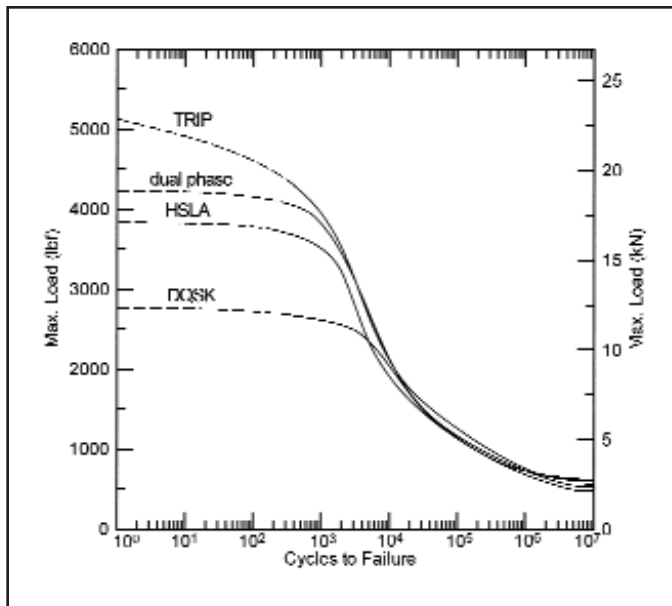


Fig. 12 — Fatigue load vs. cycles-to-failure for the tensile-shear configuration.

Fig. 13 — Fatigue load vs. cycles-to-failure for the cross-tension configuration.

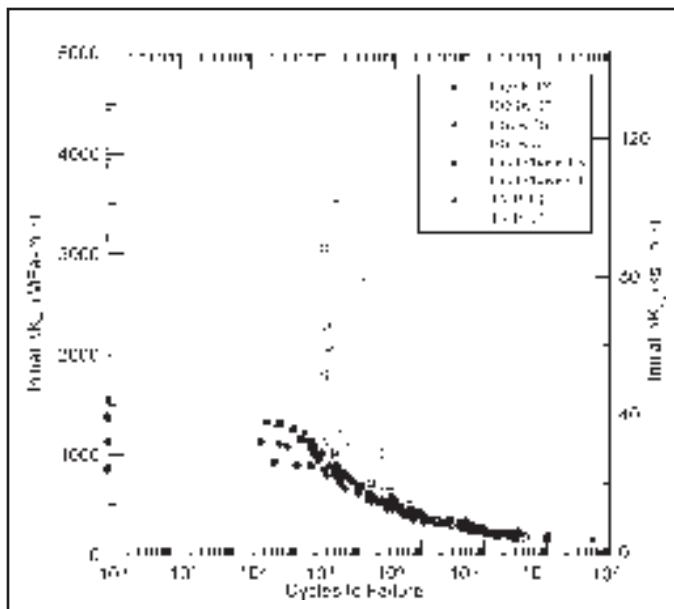


Fig. 14 — Equivalent stress intensity at initiation vs. cycles-to-failure for all materials in both the tensile-shear (TS) and cross-tension (CT) configurations.

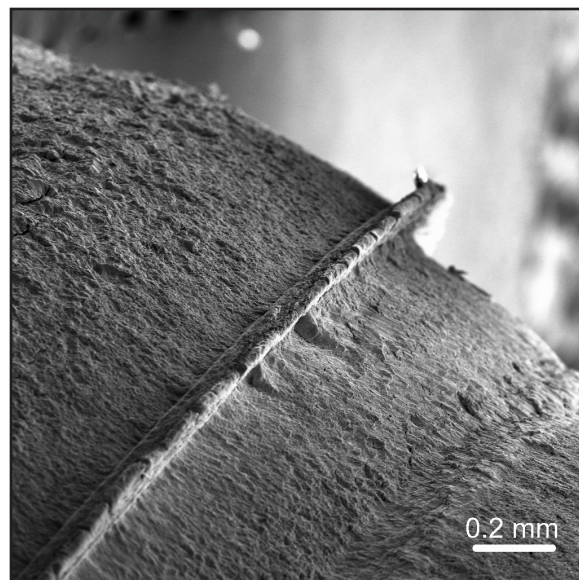


Fig. 15 — SEM of fracture surface, showing "ring" structure at sheet interface, with crack propagation outward into sheet. HSLA tested in cross-tension at 600 lb, 4000 cycles.

transition between modes was determined on the basis of the fracture characteristics, and these transitions were then compared to the fatigue curves and found to correlate with discrete regions of the curve. Beyond simply correlating with the features of the fatigue curves, these fracture modes actually control the shape of the fatigue curves. At high loads, in Type I behavior, the final failure occurs prior to the fatigue crack penetrating the sheet thickness. The overall failure occurs by tearing of the base material after net sec-

tion yielding. In this fracture mode, failure is basically due to base material failure; therefore, the fatigue curve is controlled by base material strength. Additionally, for Type I failures, a small decrease in load results in a relatively large increase in life, and the low slope of the fatigue life curves (see Fig. 8) associated with Type I failure.

In Type II behavior, the crack fully penetrated the thickness of the sheet. When the crack fully penetrated the thickness, the weld was less constrained and various rotations of the weld occurred. In the ten-

sile-shear sample, the weld rotates slightly out of plane due to eccentricity of loading applied to the partially attached button. The weld rotation increases the component of Mode I loading (i.e., crack-opening mode) at the fatigue crack tip and correspondingly increases the triaxiality of the stress state at the crack tip, thereby further increasing the crack growth rate. This contributes to the relatively steep slope in this region of the fatigue curve.

In Type III behavior, the loads are much lower, reducing weld button rota-

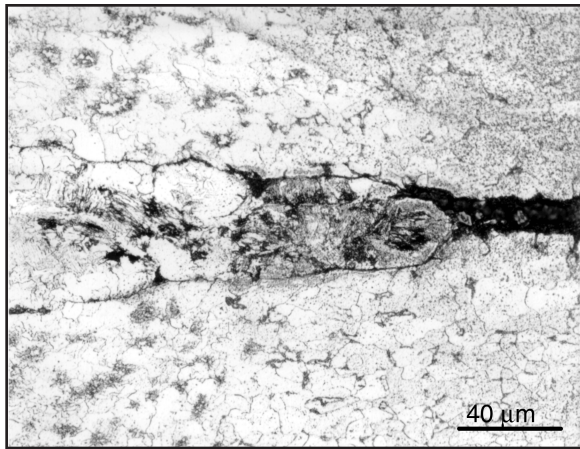


Fig. 16 — Cross section through untested weld, showing “tongue” which provides precrack. HSLA, 2% nital etch.

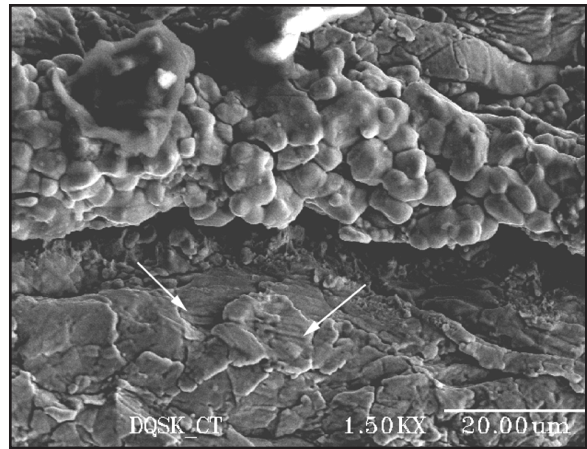


Fig. 17 — SEM image of ring, showing globular morphology and fatigue striations (marked by arrows) emanating from region. DQSK tested in cross tension at 250 lb, 110,000 cycles.

tion. Crack penetration into base material occurs as a result of the lower rotation and a corresponding reduction in the triaxiality at the crack tip as compared to Type II behavior. Thus the crack is not as strongly driven to propagate around the weld button and branches into the base material in response to the nominally applied stress. In the tensile-shear configuration, the crack is aligned perpendicular to the applied tensile stress in the sheet. In the cross-tension configuration, branching does not take on a specific orientation but is primarily driven by stresses created by the bending moment imposed by the external loads applied to the sample. The reduced triaxiality at low applied loads gives a slower crack growth rate, resulting in the flatter slope than in Region II. Additionally, the greater total crack length at failure in this region (due to the crack branching) adds to the measured fatigue life since failure was taken to be complete separation of the joint. However, the contribution due to crack branching is small as the time spent growing the branched cracks in the substrate is limited in comparison to the time spent growing the crack around the weld button.

Best-fit tensile-shear fatigue life curves for each material are compared in Fig. 12, with data points omitted for clarity. In the initial high-load region of the plot, significant differences between materials are observed. In this region, weld failure is essentially an overload failure (Type I), and therefore the differences between materials are related to base metal tensile strength. Each material transitions into Type II behavior at a different load, with higher strength materials transitioning at higher loads. However, once the materials have entered into Type II fracture behavior (i.e., above 10^3 cycles-to-failure) the curves superimpose. The fatigue curves

remain virtually identical for the different steels through the high-cycle behavior where Type III fracture behavior occurs. Throughout the transition (Region II) and high-cycle (Region III) fatigue regions of the curves, the TRIP steel gives slightly better performance, probably due to the larger weld diameters produced by the dual-pulse welding method. The DQSK steel has the highest apparent fatigue limit, defined as the load value at 10^7 cycles-to-failure, at 650 lb (2.9 kN). The TRIP steel is next at 600 lb (2.67 kN), followed by the DP steel at 550 lb (2.45 kN), and the HSLA steel has the lowest fatigue limit at 500 lb (2.2 kN).

In a previous study on the tensile-shear fatigue properties of a collection of sheet steels with tensile strengths between 30 and 95 ksi (200 and 650 MPa), Davidson (Ref. 3) reported results virtually identical to those summarized in Fig. 12. The material thicknesses and weld diameters were similar to those of this current study. At fatigue lives shorter than 10^4 cycles, higher strength materials were found to give greater fatigue performance. At higher cycles, no strength dependence of the fatigue life was found, and a fatigue limit of 550 lb (2.45 kN) was measured.

The fatigue life curves for the cross-tension configuration are shown in Fig. 13. Like the tensile-shear specimens, the cross-tension specimens also exhibit a large difference in fatigue behavior at high load. Since failure in this region is essentially overload, the relative positions of the curves for each material are related to the monotonic weld strengths shown in Table 4. In this configuration each material transitions to Type II fracture behavior at different loads, but unlike the tensile-shear results, the curves do not overlay in the 10^3 to 10^4 cycles-to-failure region. The steep slope of the curves associated with

Type II fracture behavior can be attributed to some important geometric effects. At high loads, near the Type I to Type II transition point, there is a large degree of plastic deformation in the substrate near the weld. This local plasticity alters the interfacial weld bead geometry (e.g., see Fig. 11A) at the location where fatigue cracks nucleate (as shown below, fatigue cracks nucleate in the base metal adjacent to the weld bead) effectively reducing the stress concentration factor associated with the weld/sheet interface in comparison to lower stress conditions where less “global” plasticity is encountered. The reduction in local stress concentration factor (i.e., blunting) results in longer measured fatigue lives for a given applied load.

At intermediate loads in the Type II region, where less deformation of the base metal occurs, well-developed sharp fatigue cracks grow into the base metal, and eventually the fatigue cracks fully penetrate the thickness of each sheet on opposite sides of the weld bead. The weld button then rotates out of plane, resulting in an additional moment applied at the crack tip, as shown in Fig. 11B. The moment induces an additional component of crack-opening loading at the fatigue crack tip and correspondingly increases the stress intensity applied to the fatigue crack tip. The increased stress intensity dramatically increases the crack growth rate, thereby reducing fatigue life. The combined effect of notch blunting at higher loads and the increased stress intensity at the weld due to weld button rotation at intermediate loads results in the observed shape of the fatigue life curve, where, interestingly, the slope is actually positive (i.e., decrease in life with a decrease in load) at some loads. In the region where this behavior occurs, the DQSK provides greater fatigue life, likely from increased crack blunting ef-

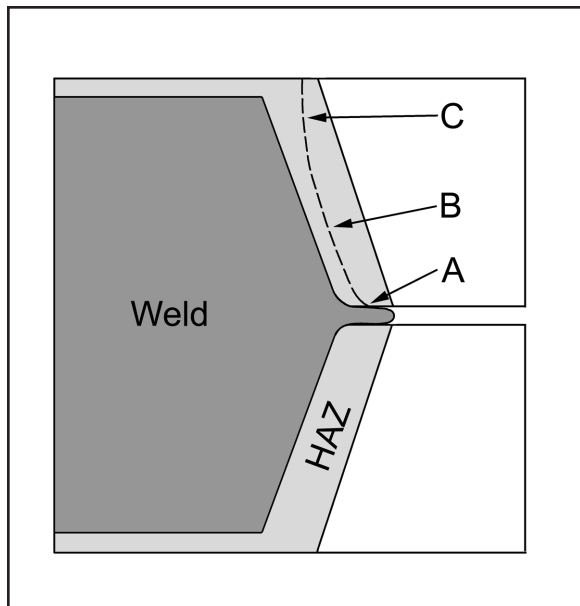


Fig. 18 — Schematic of fatigue crack propagation path (dashed line), showing (A) nucleation, (B) propagation parallel to weld interface, (C) deviation in crack path due to stress state.

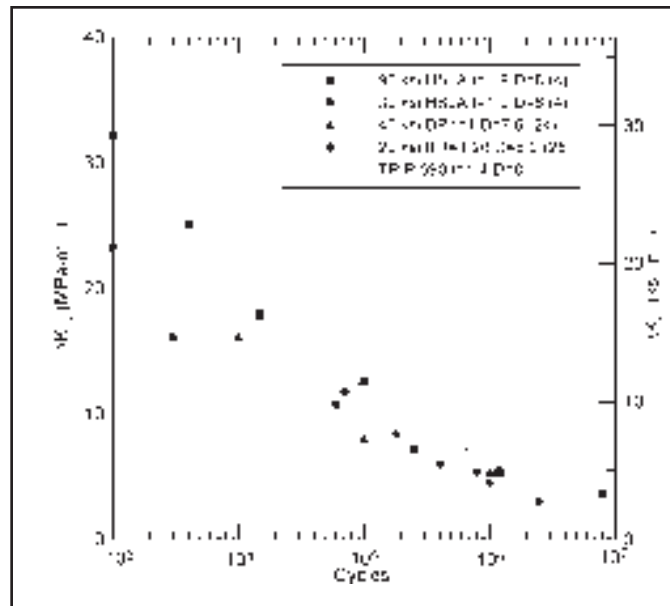


Fig. 19 — Stress intensity vs. cycles-to-failure for different materials from other studies, plotted with the TRIP material from this study. t indicates sheet thickness in mm, D indicates weld diameter in mm, and the number in parentheses is the reference number from which the data were obtained.

fects due to the low yield strength. At lower loads where Type III fracture behavior is observed, weld button rotation is minimal, life is controlled by fatigue crack propagation and the curves for each material overlap. The fatigue limit of all four materials is approximately 100 lb (0.4 kN) in this configuration, which is on the order of 4% of the static weld strength.

The fatigue strength of the TRIP steels in cross-tension loading is reduced by interfacial fracture under some conditions. At very low loads where interfacial fracture does not occur in these materials, the TRIP steel performs similarly to the other three materials. However, at intermediate loads, the fatigue strength is reduced because of interfacial fracture. If the susceptibility to interfacial fracture were reduced, it is expected that the spot welded TRIP steel would give performance at least equivalent to the other high-strength steels in all ranges of fatigue life. One potential method to reduce interfacial fracture is the application of a postweld temper cycle (Refs. 13, 19). Chuko and Gould (Ref. 19) reported that a postweld temper in the range of 60 to 80% of the expulsion current can provide an effective reduction in interfacial fracture susceptibility. Weld cycle optimization would improve the static and low-cycle fatigue strengths, although the high-cycle fatigue life would not be influenced.

Application of Fracture Mechanics Concepts

Spot weld fatigue performance results

have been shown to depend on sheet thickness and weld button size (Ref. 4). To minimize scatter in a single data set and to improve comparisons between different data sets, it has been suggested that stress intensity factors, which incorporate sample geometry, be used in place of applied loads on fatigue-life curves. Various stress intensity factor equations exist in the literature. Application of each equation requires sample and weld nugget measurements and assumptions with respect to loading direction and crack geometry. It should be noted that the application of any of these equations to the results of this study is somewhat problematic, as all assume that the sheet interface defines a crack plane parallel to the sheet surface. Implicit in these analyses is that crack growth continues in the same plane. While the fatigue cracks observed in this study nucleated at the interface between the sheets, they propagated essentially normal to the sheet, as will be shown below. Nonetheless, application of the available stress intensity factors to this study provides a valid assessment of the initial stress intensity factor prior to measurable fatigue crack growth.

Equations for K_I , K_{II} , and K_{III} (i.e., stress intensity factors for Mode I, Mode II, and Mode III loading, respectively) (Ref. 20), have recently been developed by Zhang for both the tensile-shear and cross-tension configurations (Ref. 21). Additionally, an equation for a maximum equivalent stress intensity, K_{eq} , has been developed to account for the variation in stress intensity around the weld circum-

ference. For the tensile-shear configuration, K_{eq} is given by

$$K_{eq}^{ts} = 0.694 \frac{F}{d\sqrt{t}} \quad (1a)$$

and for the cross-tension configuration by

$$K_{eq}^{ct} = 0.108 \frac{cT}{td\sqrt{t}} \quad (1b)$$

where F is the applied shear load, d is weld diameter, t is sheet thickness, c is the load span, T is applied tensile load, and the superscripts “ ts ” and “ ct ” refer to the tensile-shear and cross-tension configurations, respectively.

Figure 14 shows the initial stress intensity range, $\Delta K = K_{max} - K_{min}$, plotted vs. cycles-to-failure for all four materials and both loading configurations. In the low- to middle-cycle region, the cross-tension curves are at much higher stress intensities than the tensile-shear curves. This is due to the strong crack blunting effect described previously, which results in a calculated stress intensity significantly higher than that actually experienced by the weld in the cross-tension configuration. The ΔK vs. cycles-to-failure curves show fewer differences between materials as compared to load vs. cycles to failure. At low loads, such as those in the high-cycle region where fracture is Type III, the factors such as bending that cause deviation from the ideal behavior (on which the stress intensity equations are based) contribute little to the observed correlations. In this

region, the curves for all materials in both configurations basically superimpose, suggesting that all four materials give similar fatigue life when geometrical effects are eliminated.

Fatigue Crack Nucleation and Propagation

There has been considerable debate over the nature of fatigue crack initiation in spot welds. Some studies suggest that initiation occupies a significant portion of the fatigue life (Ref. 22, 23), whereas other studies have found that nucleation occurs immediately, with the entire fatigue life spent in crack propagation (Ref. 24). In this study, compliance measurements were used to monitor crack growth. Although the sensitivity of this method was not sufficient to determine explicitly the point of crack nucleation, the measured compliance of the specimens increased continually through the test, indicating that crack nucleation occurred immediately on loading or very early in the fatigue life and that nearly all of the life was spent in propagation (Ref. 15). The observed compliance changes were supported with direct observations of cracks in tensile-shear samples after a limited number of cycles and were observed in all tests, including long life tests (Ref. 15).

Fatigue cracks originated in all specimen configurations at a "ring" of material existing on the periphery of the weld at the sheet interface. This behavior was observed in both loading conditions but was more evident in the cross-tension samples. This material can be seen clearly in Fig. 15, a SEM photograph of the fracture surface in a cross-tension HSLA steel sample. This structure results from melted material that was forced out from the weld, forming a "tongue" along the sheet interface, as shown in the micrograph in Fig. 16. The surface is globular, oxidized due to exposure to air, and only partially melted into the base material. The tongue forms only a weak interfacial bond with the base material due to the surface oxidation. The weak interface between the tongue and the base material provides an easy fracture path and essentially creates a precrack around the weld nugget. This structure has also been identified in other studies as a source for a precrack (Ref. 25). In Fig. 17, a SEM photograph taken perpendicular to the fatigue fracture surface, the globular structure of the tongue is visible extending normal to the fracture surface in the upper portion of the figure, and fatigue striations (identified by white arrows) are visible in the lower portion of the figure emanating from the tongue structure. Remnants of the globular structure were found on mating halves of the fatigue surface.

After initiation, crack propagation occurred through the thickness of the sheet rather than along the interface parallel to the sheet surface. The characteristic fatigue crack path observed in this study is schematically correlated with the spot weld in Fig. 18, where a fatigue crack (dashed line) that nucleated at point A is shown with crack growth within the HAZ. The characteristics of crack growth associated with the three failure modes differed slightly, as discussed below. The crack initiated at the tongue structure, labeled "A." Stable fatigue crack propagation then occurred parallel to the weld interface, as shown in the region labeled "B." At lower loads, where fracture is Type II and III, the crack growth path in region "B" was at a different location in the HAZ, farther from the weld metal and closer to the unmodified base metal microstructure. In all materials, this location was between 0.010 and 0.013 in. (0.25 and 0.33 mm) from the weld interface. This region was in the intercritical region for all materials tested. This position corresponds to microhardness values in Fig. 4 of 195 HVN for the DQSK, 205 HVN for the HSLA and dual-phase steels, and 340 HVN in the TRIP steel. In Fig. 18, point "C" represents deviation in crack path due to changes in stress state around the weld resulting from loading geometry changes associated with crack growth.

Throughout the entire fatigue life, it is believed that the crack path was determined by the stress distribution around the weld as no preferred microstructural path was found. In each material, the crack propagated through microstructures of widely different strengths. The tensile strengths of the applicable intercritical HAZ microstructure, as estimated from the microhardness values given previously, range from 90 ksi (620 MPa) for the DQSK steel, 100 ksi (690 MPa) for HSLA and dual-phase steel, to 150 ksi (1000 MPa) for the TRIP steel. Despite this wide variation in strength, these materials show virtually identical crack paths and crack growth rates. During cyclic loading of spot welds, nearly the entire fatigue life was spent in stable crack growth where the crack growth rate as a function of stress intensity can be described by a Paris law function of the form $da/dN = C\Delta K^n$ (da/dN is the crack growth rate per cycle, and ΔK is the imposed stress intensity range). That the crack growth rate is similar in each material despite the differences in strength suggests that the values of C and n are similar in each material, and are independent of strength. This conclusion is consistent with the findings of Barson and Rolfe (Ref. 26), who have shown that during linear Paris law crack growth, crack growth rates are dependent only on microstructure type (e.g.,

ferrite-pearlite vs. martensite), and independent of the strength of the microstructure. For example, Barson and Rolfe (Ref. 26) showed that the fatigue crack growth rate vs. ΔK curve for a group of quenched and tempered martensitic steels with yield strengths in the range of 560 to 2100 MPa (80 to 300 ksi) were described by a single pair of C and n values. Correspondingly, a different pair of values was obtained for ferrite-pearlite steels. These previous results suggest that the microstructure that controls fatigue crack growth is the local crack-tip microstructure, i.e., the initial microstructure as modified by a large number of strain cycles within the plastic zone ahead of the fatigue crack. Furthermore, these results suggest that the local microstructure immediately ahead of a propagating crack develops characteristic structure and properties for a given material class (e.g., martensitic steels) independent of the initial strength level.

Comparisons with Previously Published Spot Weld Fatigue Data

Although the samples in this study were all of similar thickness and weld diameter, the use of a fracture mechanics based approach should allow an accurate comparison of fatigue performance from tests on samples with different sheet thicknesses, weld diameters, load ratios, and sample configurations. Using Equation 1a, equivalent stress intensity values were calculated for tensile-shear samples from several previous studies (Refs. 4, 27, 28) where load vs. cycles-to-failure data were available, typically only for fatigue lives greater than 10^3 . The materials range from a 20 ksi (130 MPa) IF steel to a 90 ksi (600 MPa) HSLA steel, with sheet thicknesses from 1.0 to 1.9 mm (0.04 to 0.075 in.), and weld diameters ranging from 6.2 to 8 mm (0.24 to 0.31 in.). The calculated values of ΔK_{eq} for these materials, together with data for the TRIP steel from the current study, are plotted vs. measured fatigue lives in Fig. 19. Note that for clarity, only one set of data from the current study is included in Fig. 19, as Fig. 14 illustrated that at the lower imposed loads all data from the current study were similar. Considering that the materials are greatly different, that the geometries vary widely, and that different researchers conducted the tests, the correspondence between curves is excellent. All of the materials provide nearly equal fatigue performance when the effects of geometric differences are eliminated through the use of stress intensity factor calculations. The differences between materials in a load vs. cycles-to-failure plot are primarily due to geometric differences. Therefore, the high-cycle fatigue performance is independent of base material microstructure.

ture and strength, and the fatigue performance is controlled almost exclusively by sample geometry.

Conclusions

At low cycles and high loads, high-strength steels provide superior spot weld fatigue performance, with performance related directly to the spot weld overload strength. At intermediate loads, similar behavior was observed for all four steels tested in the tensile-shear configuration. However, for the cross-tension samples a unique behavior was observed for the higher-strength steels where the fatigue life actually decreased with a decrease in load — behavior attributed to geometrical effects. At low loads and high cycles, spot weld fatigue performance is independent of base material strength or microstructure. Although the static overload weld strength of the TRIP material in the cross-tension configuration was reduced due to interfacial fracture, at low loads the TRIP material provided a fatigue strength equal to the other materials. In all materials, fatigue cracks nucleated at a tongue structure at the sheet interface that resulted from molten material forced out from the weld nugget. The tongue provides a pre-crack for fatigue, and crack growth initiates immediately upon loading. Crack propagation in all materials occurred in an intercritical region of the HAZ, with the path determined by the stress distribution at the nugget. Analysis based on stress intensity factor calculations demonstrated that at low loads and high cycles, the tensile-shear and cross-tension configurations provide equal performance. Analysis of data from several previous spot weld fatigue studies showed that, using stress intensity factor calculations to account for variations in sample geometry, all spot welded steels provide essentially identical high-cycle, low-load fatigue performance. Thus, it is concluded that high-cycle spot weld fatigue performance of the automotive sheet steels considered in this paper is determined by geometric factors, rather than material strength or microstructure, even for the high-strength TRIP steel, which exhibited components of interfacial fracture in the high-strength weld metal when tested at high loads in the low-life regime.

Acknowledgments

The authors acknowledge the support of the Advanced Steel Processing and Products Research Center, an NSF Industry-University Cooperative research center at the Colorado School of Mines. The authors thank Ispat-Inland, National Steel, and POSCO for supplying the experimental materials, and Daimler-Chrysler for assistance in spot welding of test samples.

References

- Shaw, J., Engl, B., Espina, C., Oren, E. C., and Kawamoto, Y. 2002. *ULSAB — advanced vehicle concepts — materials*. SAE Technical Paper 2002-01-0044. Warrendale, Pa.: Society of Automotive Engineers.
- American Iron and Steel Institute. 1998. *Ultralight steel auto body final report*.
- Davidson, J. A., and Imhof, E. J. Jr., 1984. *The effect of tensile strength on the fatigue life of spot-welded sheet steels*. SAE Technical Paper 840110. Warrendale, Pa.: Society of Automotive Engineers.
- Davidson, J. A. 1983. *A review of the fatigue properties of spot-welded sheet steels*. SAE Technical Paper 830033. Warrendale, Pa.: Society of Automotive Engineers.
- Davidson, J. A. 1983. *A fracture-mechanics and system-stiffness approach to fatigue performance of spot-welded sheet steels*. SAE Technical Paper 830034. Warrendale, Pa.: Society of Automotive Engineers.
- DeCooman, B. C., ed. 2002. *Proceedings of the International Conference on TRIP-Aided High Strength Ferrous Alloys*. 1–386. Bad Harzburg, Germany: Garbracht Redaktions und Industrie Presse Service.
- Cooper, J. F., and Smith, R. A. 1986. Fatigue crack propagation at spot welds. *Metal Construction* 18(6): 383R–386R.
- Speer, J. G., and Matlock, D. K. 2002. Recent developments in low-carbon sheet steels. *JOM* 54(7): 19–24.
- Matlock, D. K., Krauss, G., and Zia-Ebrahimi, F. 1984. Strain hardening of dual-phase steels: An evaluation of the importance of processing history. *Deformation, Processing, and Structure*. Ed. G. Krauss. 47–87. Metals Park, Ohio: ASM.
- Olson, G. B. 1984. Transformation plasticity and the stability of plastic flow. *Deformation, processing, and Structure*, ed. G. Krauss, 391–424. Metals Park, Ohio: ASM.
- Sakuma, Y., Matlock, D. K., and Krauss, G. 1992. Intercritically annealed and isothermally transformed 0.15 pct C steels containing 1.2 pct Si-1.5 pct Mn and 4 pct Ni: Part I. Transformation, microstructure, and room temperature mechanical properties. *Metallurgical Transactions A* 23A: 1221–32.
- Gallagher, M. F., Speer, J. G., Matlock, D. K., and Fonstein, N. M. 2002 (Sept.). Microstructure development in TRIP-sheet steels containing Si, Al, and P. *Proceedings of the 43rd Mechanical Working and Steel Processing Conference*, 153–72. Warrendale, Pa.: ISS-AIME.
- Cretteur, L., Koruk, A. I., and Tosal-Martinez, L. 2002. Improvements of weldability of TRIP steels by use of in-situ pre- and post-heat treatments. *Proceedings of the International Conference on TRIP-Aided High Strength Ferrous Alloys*, ed. B. C. DeCooman, 353–358. Bad Harzburg, Germany: Garbracht Redaktions und Industrie Presse Service.
- Cieslak, M. J. 1990. Cracking phenomena associated with welding. In *ASM Handbook*. Vol. 6, Welding, Brazing, and Soldering, p. 94. Materials Park, Ohio: ASM International.
- Rathbun, R. W. 2002. Fatigue behavior of spot-welded high strength sheet steels. Master's thesis, Colorado School of Mines, Golden, Colo.
- Japanese Standards Association. *Method of fatigue testing for spot-welded joint*. JIS Z 3138:1989.
- O'Brien, R. L., ed. 1991. *Welding Hand- book*. Vol. 2, Welding Processes, 532–79. Miami, Fla.: American Welding Society.
- Gould, J. E., and Workman, D. 1998. Fracture morphologies of resistance spot welds exhibiting hold time sensitivity behavior. *Eighth Sheet Metal Working Conference*. Miami, Fla.: American Welding Society.
- Chuko, W. L., and Gould, J. E. 2002. Development of appropriate resistance spot-welding practice for transformation hardened steels. *Welding Journal* 81(1): 1–s to 7–s.
- Dieter, G. E. 1986. *Mechanical Metallurgy*, 3rd ed., p. 352. New York: McGraw Hill.
- Zhang, S. 1997. Stress intensities at spot welds. *International Journal of Fracture* 88:167–85.
- Lawrence, F. V., Wang, P. C., and Corten, H. T. 1983. *An empirical method for estimating the fatigue resistance of tensile-shear spot welds*. SAE Technical Paper 830035. Warrendale, Pa.: Society of Automotive Engineers.
- Sheppard, S. D., and Strange, M. 1992. Fatigue life estimation in resistance spot welds: Initiation and early growth phase. *Fatigue and Fracture of Engineering Materials and Structures* 15(6): 531–49.
- Cooper, J. F., and Smith, R. A. 1986. Fatigue crack propagation at spot welds. *Metal Construction* 18(6): 383R–386R.
- Hamel, F. G., and Masounave, J. 1990. The fatigue behavior of HSLA non-load carrying spot-welded joints. *Canadian Metallurgical Quarterly* 29(4): 313–18.
- Barson, J. M., and Rolfe, S. T. 1999. *Fracture and Fatigue Control in Structures*. 200–204. West Conshohocken, Pa.: ASTM.
- Sperle, J. O. 1983. Strength of spot welds in high strength steel sheet. *Metal Construction* 15(4): 200–203.
- Allen, B., and Applegate, D. 2000. *The effects of boron and stabilization chemistry on the spot-weld fatigue and secondary cold work embrittlement of hot dip galvanized interstitial-free steels*. SAE Technical Paper 2000-01-2700. Warrendale, Pa.: Society of Automotive Engineers.

Change of Address? Moving?

Make sure delivery of your *Welding Journal* is not interrupted. Contact the Membership Department with your new address information — (800) 443-9353, ext. 480; jeon@aws.org.